

Magnetic structures and electronic properties of cubic-pyrochlore ruthenates from first principles

M.-T. Huebsch^{1,2}, Y. Nomura¹, S. Sakai¹ and R. Arita^{1,3}

¹Center for Emergent Matter Science, RIKEN, Wako, Saitama 351-0198, Japan

²VASP Software GmbH, Sensengasse 8/17, A-1090 Vienna, Austria

³University of Tokyo, 7-3-1 Hongo, Bunkyo-ku, Tokyo 113-8656, Japan

E-mail: marie-therese.huebsch@vasp.at

Abstract. The magnetic ground states of $R_2\text{Ru}_2\text{O}_7$ and $A_2\text{Ru}_2\text{O}_7$ with $R = \text{Pr, Gd, Ho, and Er}$, as well as $A = \text{Ca, Cd}$ are predicted devising a combination of the cluster-multipole (CMP) theory and spin-density-functional theory (SDFT). The strong electronic correlation effects are estimated by the constrained-random-phase approximation (cRPA) and taken into account within the dynamical-mean-field theory (DMFT). The target compounds feature d -orbital magnetism on Ru^{4+} and Ru^{5+} ions for R and A , respectively, as well as f -orbital magnetism on the R site, which leads to an intriguing interplay of magnetic interactions in a strongly correlated system. We find CMP+SDFT is capable of describing the magnetic ground states in these compounds. The cRPA captures a difference in the screening strength between $R_2\text{Ru}_2\text{O}_7$ and $A_2\text{Ru}_2\text{O}_7$ compounds, which leads to a qualitative and quantitative understanding of the electronic properties within DMFT.

Keywords: noncollinear magnetism, first-principles calculations, strongly correlated electron system

Submitted to: *J. Phys.: Condens. Matter*

1. Introduction

Cubic-pyrochlore ruthenates [1, 2] are subject to magnetic frustration, strong electronic correlation, and in some cases a considerable amount of spin-orbit coupling (SOC). Consequently, this family of materials, that has the chemical formula $(R_{1-x}A_x)_2\text{Ru}_2\text{O}_7$, displays a plethora of different phases and transitions, including the Mott-insulating state, bad metal state, spin-ice-like states and other noncollinear magnetism. The ground state strongly depends on the choice of cations A^{2+} and R^{3+} . Yet, in addition to that, different phases can be reached by introducing hole doping x [3, 4] or by applying pressure [5]. Curiously, the experimentally observed tendencies with changing conditions are sometimes counter-intuitive, as described below. Here, we demonstrate that first-principles calculations can help elucidate the underlying phenomena of these counter-intuitive tendencies.

In $(R_{1-x}A_x)_2\text{Ru}_2\text{O}_7$, magnetic frustration arises from the corner sharing tetrahedra formed by both, R and Ru sites, as shown in Figure 1 (a). The crystallographic details can be seen at a glance in Table 1. In particular, we will consider the cases with a magnetic rare-earth ion $R^{3+} = \text{Pr}, \text{Gd}, \text{Ho}$ and Er , and with a nonmagnetic cation $A^{2+} = \text{Ca}$, and Cd in details. This choice covers a wide range of magnetic and electronic phases with different prevalent mechanisms.

For rare-earth ruthenates, $R_2\text{Ru}_2\text{O}_7$, the cubic-pyrochlore structure amounts to an interesting constellation of two magnetically coupled frustrated sublattices at $16c$ and $16d$, that are dominated by d -orbital and f -orbital magnetism, respectively. In contrast, in $A_2\text{Ru}_2\text{O}_7$ only one magnetic site, i.e., the Ru site, exists. Still, as discussed in Section 2, the d -orbital magnetism is fundamentally different in the limiting cases of $(R_{1-x}A_x)_2\text{Ru}_2\text{O}_7$ owing to an effective integer and half-integer spin state on the Ru site.

Capturing the subtleties of cubic-pyrochlore ruthenates on the experimental side is a challenge in itself, as indicated by the relatively recently successful synthesis, low transition temperatures and remaining uncertainties of the magnetic-structure measurements, c.f., Section 2. A prominent example of the possible magnetic configurations is the spin-ice structure which is characterized by its magnetic entropy [6, 7]. Regarding the electronic properties,

recent advances by Kaneko *et al.* [4] made it possible to investigate fully filling-controlled $(\text{Ca}_{1-x}\text{Pr}_x)_2\text{Ru}_2\text{O}_7$, which shows a metal-to-insulator transition (MIT), where surprisingly $\text{Pr}_2\text{Ru}_2\text{O}_7$ is a Mott insulator and $\text{Ca}_2\text{Ru}_2\text{O}_7$ is a metal. This is unexpected because the valence- t_{2g} bands within the $\text{Ru-}4d^3$ manifold are half-filled for $A_2\text{Ru}_2\text{O}_7$, which naively should observe higher electronic correlation compared to the more than half-filled $\text{Ru-}4d^4$ bands in $R_2\text{Ru}_2\text{O}_7$ [8]. Moreover, Jiao *et al.* [5] demonstrated that $\text{Cd}_2\text{Ru}_2\text{O}_7$ is driven from metal to insulator by increasing pressure, in stark contrast to the related monoclinic compound $\text{Hg}_2\text{Ru}_2\text{O}_7$, which is a bad metal and becomes a good metal under pressure [9]. Again, the behavior of $\text{Cd}_2\text{Ru}_2\text{O}_7$ is counter-intuitive, as without a structural transition the overlap integral between neighboring sites is expected to increase with pressure and, thus, electrons can more easily hop from one site to another, which increases their itinerancy.

These experimental findings suggest a need to carefully treat strong electronic correlation effects in these systems. Thus, we will go beyond spin-density-functional theory [10] (SDFT) and additionally employ the dynamical-mean-field theory [11] (DMFT). Yet, in order to truly remain a first-principles calculation, i.e., avoid free parameters, we obtain all the parameters used in the DMFT calculation by means of the constrained-random-phase approximation (cRPA) [12].

In the remainder of this paper, we focus on the magnetic structure and electronic properties of $R_2\text{Ru}_2\text{O}_7$ with $R^{3+} = \text{Pr}, \text{Gd}, \text{Ho}$, and Er , as well as $A_2\text{Ru}_2\text{O}_7$ with nonmagnetic $A^{2+} = \text{Ca}$, and Cd . First, we predict the magnetic ground state from first-principles devising the so-called cluster-multipole (CMP)+SDFT magnetic-structure-prediction scheme [13] and show that Ca and Cd compounds have robust all-in-all-out (AIAO) magnetic order within SDFT. Furthermore, for $R_2\text{Ru}_2\text{O}_7$, we find that different magnetic configurations are competing depending on the rare-earth element, which is consistent with experimental results. In particular, for $\text{Ho}_2\text{Ru}_2\text{O}_7$, we find a spin-ice-like state, while the remaining compounds prefer an antiferromagnetic (AFM) 32-pole structure. Beyond that, cRPA calculations reveal that the relative energy of the $\text{O-}2p$ and $\text{O'-}2p$ bands \ddagger with respect to the $\text{Ru-}t_{2g}$ bands controls

\ddagger The $\text{O-}2p$ and $\text{O'-}2p$ orbitals are on the $48f$ and $8b$ site, respectively, as shown in Table 1 and Figure 1.

Table 1. Crystallographic positions for the space group $Fd\bar{3}m$ (No. 227) of the cubic-pyrochlore structure $(R_{1-x}A_x)_2\text{Ru}_2\text{O}_6\text{O}'$ with origin at $16c$. The parameter x_a is the only compound-dependent parameter, apart from the lattice constant a . For more details about the crystallographic information, we refer to Ref. [1].

Atom	Wyckoff position	Site symmetry	Coordinate
A/R	$16d$	$\bar{3}m(D_{3d})$	$\frac{1}{2}, \frac{1}{2}, \frac{1}{2}$
Ru	$16c$	$3m(D_{3d})$	$0, 0, 0$
O	$48f$	$mm(C_{2v})$	$x_a, \frac{1}{8}, \frac{1}{8}$
O'	$8b$	$\bar{4}3m(T_d)$	$\frac{3}{8}, \frac{3}{8}, \frac{3}{8}$

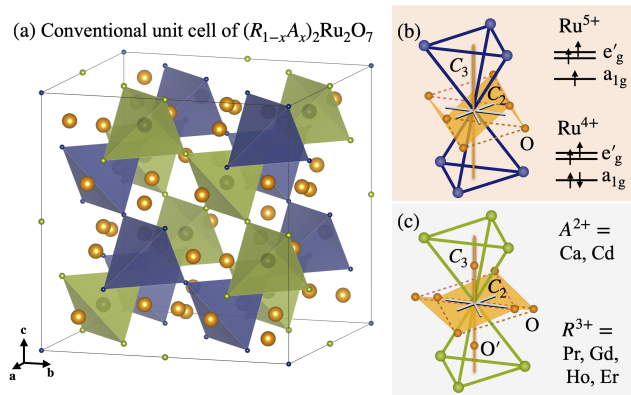


Figure 1. Crystal structure of $(R_{1-x}A_x)_2\text{Ru}_2\text{O}_6\text{O}'$. (a) Conventional unit cell showing the cubic-pyrochlore Ru (R/A) sublattice in blue (green) and O in orange. O' is located inside the green R/A tetrahedra. (b) and (c) show the local environment of Ru and R/A , which both display $\bar{3}m(D_{3d})$ site symmetry. The crystal-electric-field splitting and occupancy of the $\text{Ru-}t_{2g}$ manifold into a lower a_{1g} and upper e'_g bands for Ru^{5+} (Ru^{4+}) that occurs for the choice of A (R) element is depicted at the top (bottom), in (b) and (c) respectively.

the screening of the on-site Coulomb repulsion U and it differs significantly between $\text{Ru-}4d^3$ and $\text{Ru-}4d^4$ compounds. This explains the counter-intuitive reduction of the electronic correlation in the half-filled $\text{Ru-}4d^3$ - t_{2g} bands in $\text{A}_2\text{Ru}_2\text{O}_7$ compared to $\text{Ru-}4d^4$ bands in $\text{R}_2\text{Ru}_2\text{O}_7$. Lastly, we compute the electronic properties for $\text{Ca}_2\text{Ru}_2\text{O}_7$ and $\text{Pr}_2\text{Ru}_2\text{O}_7$ within DMFT using model parameters extracted from first-principles calculations by means of cRPA. The results show a bad metallic behavior for $\text{Ca}_2\text{Ru}_2\text{O}_7$ consistent with experimental results. Moreover, for $\text{Pr}_2\text{Ru}_2\text{O}_7$ a band gap opens, which is qualitatively and quantitatively in agreement with experimental results.

2. Magnetic structure

Let us start by developing some intuition about the competing magnetic interactions. As mentioned in the introduction, for $\text{R}_2\text{Ru}_2\text{O}_7$, the cubic-pyrochlore structure comprises two magnetically coupled frustrated sublattices at $16c$ and $16d$, that are dominated by d -orbital and f -orbital magnetism, respectively. This is

shown in Figure 1 (a).

The d -orbital magnetism arises from the $\text{Ru-}4d^4$ bands in $\text{R}_2\text{Ru}_2\text{O}_7$, which host 4 electrons in the ionic limit. The exchange interaction between neighboring Ru moments is expected to be dominant compared to, e.g., dipole-dipole interactions. That is, because the on-site magnetic dipole moments on the Ru site are relatively small even if the high-spin state were realized, and the orbital-angular momentum \mathbf{L} is likely quenched by the crystal-electric-field (CEF) splitting. Therefore, SOC is suppressed on the Ru site in all compounds investigated here. According to ligand-field theory [14], the overall cubic (O_h) symmetry splits the $\text{Ru-}4d$ bands into lower lying t_{2g} and upper e_g bands. The former is further split into a lower a_{1g} and upper e'_g bands due to the local trigonal (D_{3d}) symmetry. This yields a spin $S = 1$ state in the $\text{Ru-}4d^4$ manifold for $\text{R}_2\text{Ru}_2\text{O}_7$, as shown in Figure 1 (b) bottom.

On the other hand, in the case of f -orbital magnetism, the electrons are more localized and, thus, better shielded from the surrounding CEF. Consequently, almost no quenching occurs and the heavy nuclei give rise to substantial SOC. One exception is given by the half-filled f -bands, where $\mathbf{L} = 0$ for the ideal case of R^{3+} . In particular, in the compounds investigated here, SOC is expected to increase from $\text{R}^{3+} = \text{Gd, Pr}$ to Er and Ho . The ordering of the latter two cannot be predicted *a priori* due to its dependence on multiple variables, whose values are expected to be of similar magnitude. For instance, SOC depends on the mass of the nuclei, the spin and angular contributions to the on-site magnetic moment. As shown in Figure 1 (c), the $4f$ bands on the $16d$ - R site observe a D_{3d} -site symmetry, which slightly lifts the local $2J + 1$ degeneracy of the $4f^n$ manifold. Here, J is the total-angular-momentum-quantum number of n electrons that occupy the $4f$ orbitals on the R site.

The R moment is expected to increase from Pr , Gd , Er to Ho when considering the J - J coupling scheme, while the ionic radius ratio r_R/r_{Ru} decreases from Pr , Gd , Ho to Er §. Note that, the d -

§ According to Figure 12 in Ref. [15], the values of the ionic

Table 2. Basis configurations (BCs) of the cluster-multipole (CMP) basis for the cubic-pyrochlore structure $(R_{1-x}A_x)_2\text{Ru}_2\text{O}_6\text{O}'$ with origin at 16c according to their multipole order and irreducible representation (IRREP). With Ru/ $R_{1-x}A_x$ at positions of Atom 1: $(0, 0, 0)/(1/2, 1/2, 1/2)$, Atom 2: $(1/4, 1/4, 0)/(3/4, 3/4, 1/2)$, Atom 3: $(1/4, 0, 1/4)/(3/4, 1/2, 3/4)$, and Atom 4: $(0, 1/4, 1/4)/(1/2, 3/4, 3/4)$. The BCs are depicted in Figure 1. Note that, the BCs of Γ_{1g} and Γ_{2g} are different domains of the same magnetic structure.

Multipole	IRREP	BC	Atom 1	Atom 2	Atom 3	Atom 4
dipole	Γ_9 (T_{1g})	Ψ_1	(1, 0, 0)	(1, 0, 0)	(1, 0, 0)	(1, 0, 0)
		Ψ_2	(0, 1, 0)	(0, 1, 0)	(0, 1, 0)	(0, 1, 0)
		Ψ_3	(0, 0, 1)	(0, 0, 1)	(0, 0, 1)	(0, 0, 1)
octupole	Γ_3 (A_{2g})	$\sqrt{3}\Psi_4$	(-1, -1, -1)	(1, 1, -1)	(1, -1, 1)	(-1, 1, 1)
	Γ_9 (T_{1g})	$\sqrt{2}\Psi_5$	(0, 1, 1)	(0, 1, -1)	(0, -1, 1)	(0, -1, -1)
		$\sqrt{2}\Psi_6$	(1, 0, 1)	(1, 0, -1)	(-1, 0, -1)	(-1, 0, 1)
		$\sqrt{2}\Psi_7$	(1, 1, 0)	(-1, -1, 0)	(1, -1, 0)	(-1, 1, 0)
	Γ_7 (T_{2g})	$\sqrt{2}\Psi_8$	(0, -1, 1)	(0, -1, -1)	(0, 1, 1)	(0, 1, -1)
		$\sqrt{2}\Psi_9$	(1, 0, -1)	(1, 0, 1)	(-1, 0, 1)	(-1, 0, -1)
		$\sqrt{2}\Psi_{10}$	(-1, 1, 0)	(1, -1, 0)	(-1, -1, 0)	(1, 1, 0)
	Γ_5 (E_g)	$\sqrt{2}\Psi_{11}$	(-1, 1, 0)	(1, -1, 0)	(1, 1, 0)	(-1, -1, 0)
		$\sqrt{6}\Psi_{12}$	(-1, -1, 2)	(1, 1, 2)	(1, -1, -2)	(-1, 1, -2)

f exchange interaction is expected to be large compared to f - f exchange interaction due to the strong localization of the f electrons. Intriguingly, the dipole-dipole interaction between R moments may also play an important role between large on-site magnetic moments, as can emerge on the Ho and Er sites. This is seen in the related isostructural spin-ice compound $\text{Ho}_2\text{Tb}_2\text{O}_7$ [16, 17, 6] and can lead to an effective ferromagnetic (FM) nearest-neighbor interaction, even if the exchange interaction is AFM.

In contrast, $A_2\text{Ru}_2\text{O}_7$ only features one magnetic site, i.e., the Ru site. The presence of A^{2+} leads to a higher oxidation state Ru^{5+} in the ionic limit. This in turn permits only 3 electrons in the $\text{Ru}-4d^3\text{-}a_{1g}$ and $\text{Ru}-4d^3\text{-}e'_g$ bands, whose spins are expected to form a high-spin $S = 3/2$ state according to Hund's rules, as illustrated in Figure 1 (b) top. This stands in contrast with $R_2\text{Ru}_2\text{O}_7$, where Ru^{4+} yields an $S = 1$ state in the $\text{Ru}-4d^4$ manifold. Consequently, even the undisturbed formation of magnetism on the Ru site is fundamentally different in $A_2\text{Ru}_2\text{O}_7$ compared to $R_2\text{Ru}_2\text{O}_7$. In other words, the magnetism on the Ru site in $A_2\text{Ru}_2\text{O}_7$ and $R_2\text{Ru}_2\text{O}_7$ must be discussed separately for two reasons: (i) the different state of oxidation, and (ii) the possible interaction with a second magnetic lattice formed by R sites.

Recently, magnetic multipoles are increasingly used to describe magnetic states in condensed matter on an atomic scale [18, 19, 20, 21], as well as on an inter-atomic scale [22, 23, 24, 25, 26, 27]. This has led to the formulation of the so-called CMP theory [28], that proposes a basis to span the space of all possible magnetic configurations in a crystal in terms of

radius ratio are approximately 1.81, 1.69, 1.63 and 1.61 for $R=\text{Pr}$, Gd , Ho and Er , respectively. In case of $A_2\text{Ru}_2\text{O}_7$, Figure 25 in Ref. [15] yields 1.95 and 1.97 for $A=\text{Cd}$, and Ca .

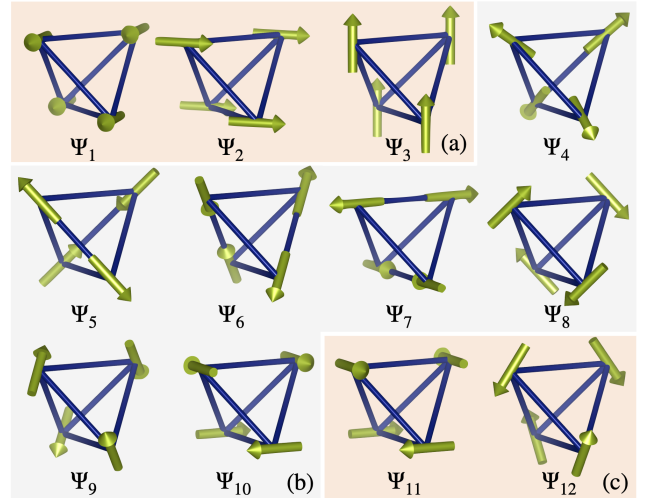


Figure 2. Cluster-multipole (CMP) basis. (a) Dipole basis configurations (BCs), (b) Octupole BCs, and (c) 32-pole BCs. As listed in Table 2, the BCs of the CMP basis are associated with an irreducible representation (IRREP), i.e., Ψ_1, Ψ_2, Ψ_3 , as well as Ψ_5, Ψ_6, Ψ_7 are $\Gamma_9(T_{1g})$, Ψ_4 is $\Gamma_3(A_{2g})$, $\Psi_8, \Psi_9, \Psi_{10}$ are $\Gamma_7(T_{2g})$, and Ψ_{11}, Ψ_{12} are $\Gamma_5(E_g)$. Note that, (i) Ψ_4 corresponds to the all-in-all-out (AIAO) structure, (ii) the spin-ice 2-in-2-out structure is a linear combination of dipole and octupole of IRREP $\Gamma_9(T_{1g})$, e.g., $(\Psi_1 + \Psi_5)/\sqrt{2}$.

magnetic multipoles. The magnetic configurations that form the CMP basis of cubic-pyrochlore ruthenates are explicitly given in Table 2.

In Figure 2, the 12 basis configurations (BCs) are depicted. These comprise dipoles, octupoles and 32 poles \parallel . By construction, each BC additionally

\parallel We note that CMP theory can equally well define magnetic configurations corresponding to magnetic toroidal multipole moments. However, as the magnetic field is by construction an expansion of magnetic multipoles and we are not referring

corresponds to a specific irreducible representation (IRREP) of the magnetic point group.

It is well-known that most magnetic structures can be described with one IRREP, which can be understood in the context of Landau theory of second-order phase transitions [29]. That is why Rietveld fits [30] to neutron diffraction patterns are usually performed with a basis similar to the CMP basis as a starting point [31, 32, 33, 34, 35, 36], which however lacks the characterization in terms of magnetic multipoles. The additional characterization of magnetic multipoles has two main advantages: First, it is rather intuitive that the complexity of the magnetic structure increases with the magnetic multipole order. Second, the shape of the linear response tensor can be directly inferred [20]. For instance, the CMP theory has been instrumental in understanding the large anomalous Hall effect in the noncollinear AFM compound Mn_3Sn [24, 27].

Motivated by this success, some of the present authors developed a systematic scheme [13] to predict the magnetic ground state from first principles for a given crystal structure based on the CMP theory and SDFT. The predictive power of this scheme, that is termed CMP+SDFT [13], has been demonstrated in a high-throughput calculation of more than 4400 SDFT calculations. The key issue, that was overcome, is that SDFT has many local minima in its total-energy landscape. An exhaustive list of candidate magnetic structures is instrumental to converge to all relevant (meta-)stable magnetic structures. To this end, we follow a statistically justified heuristic rule and take equally weighted linear combinations of all BCs with the same IRREP and multipole order. Note, that in the cubic-pyrochlore structure, the BCs of T_{1g} and T_{2g} are actually different domains of the same magnetic structure. In other words, they are related to each other by an alternative choice of the lattice vector and are degenerate by symmetry. That is, they will yield the same total energy in SDFT.

After eradicating such redundant initial candidate magnetic configurations, we perform SDFT calculations using the Vienna *ab-initio* simulation package (VASP) [37, 38, 39]. We employ the pseudopotentials of the projector-augmented-waves (PAW) method version potpaw54 titled Ca_sv, Cd, Pr, Gd, Ho, Er, O, and Ru_pv in combination with the Perdew-Burke-Ernzerhof (PBE) exchange-correlation functional to converge the Kohn-Sham (KS) orbitals with the cutoff energy set to 520 eV in a self-consistency loop considering SOC [40] and noncollinear magnetism in the sense of J Kuebler's formulation of SDFT [10], where the KS Hamiltonian can be locally diagonalized. That is,

to effects where electrons couple to the gauge field, we choose to focus on magnetic multipoles here, in contrast to Ref. [28]

the magnetic moments are not fixed during the self-consistent calculation. We use a \mathbf{k} mesh of $4 \times 4 \times 4$ devising the Monkhorst-Pack scheme and the structures that are listed in the inorganic crystal structure database [41] under the ids 156409, 86773, 163397, 79332, 96730, and 97533. Note that we use the experimental crystal-structure information without performing additional ionic relaxation. It is provided along with the magnetic structure in the supplemental material. For more details of the VASP calculations see Ref. [13], where we used the same computational procedure.

2.1. Magnetic structure of $A_2\text{Ru}_2\text{O}_7$

After $\text{Cd}_2\text{Ru}_2\text{O}_7$ [42] in 1998, $\text{Ca}_2\text{Ru}_2\text{O}_7$ [43] could be synthesized in 2006. Finally, also $\text{Hg}_2\text{Ru}_2\text{O}_7$ [44, 45] got synthesized in 2007, however it undergoes a structural phase transition [46] from cubic to monoclinic at the same time as the Ru moments order at 107K, which yields Kagome-like layers instead of corner-sharing tetrahedra. That is why, we focus on $\text{Ca}_2\text{Ru}_2\text{O}_7$ and $\text{Cd}_2\text{Ru}_2\text{O}_7$ in the CMP+SDFT calculations below..

While to our knowledge there is no experimental data available that directly probes the magnetic order in $\text{Ca}_2\text{Ru}_2\text{O}_7$ and $\text{Cd}_2\text{Ru}_2\text{O}_7$, some magnetic properties can be found in the literature. The specific heat reveals distinct λ anomalies at $T_N \approx 85$ K for $\text{Cd}_2\text{Ru}_2\text{O}_7$ [5], and at $T_N \approx 107$ K for $\text{Hg}_2\text{Ru}_2\text{O}_7$ [45]. These anomalies are associated with a second-order phase transition at which the Ru moments order. To our knowledge the specific heat for $\text{Ca}_2\text{Ru}_2\text{O}_7$ has not been reported. At zero-field no net magnetization is observed, so that the magnetic structures are all either AFM or glasslike.

Further, the zero-field cooled (ZFC) magnetic susceptibility with $A = \text{Cd}$ [47, 5] and Hg [45] shows sharp cusps at T_N , and a speculative *spin-glass* transition at $T_g \approx 25$ K for $A = \text{Ca}$ [43, 48]. This further confirms that a magnetic transition occurs. For $\text{Cd}_2\text{Ru}_2\text{O}_7$ no high-temperature Curie-Weiss behavior is observed, but instead a broad maximum is stretched over a wide temperature range [42, 5]. This is similar to $\text{CaCu}_3\text{Ru}_4\text{O}_{12}$, which can be discussed in terms of a high Kondo temperature which implies the presence of spin-fluctuations in a strongly-correlated-electron system [49]. Additionally, the magnetic susceptibility of $\text{Cd}_2\text{Ru}_2\text{O}_7$ seems to reveal a second and third *magnetic* transitions around $T_m \approx 40$ K and $T_{m2} \approx 25$ K [5], which are indicated by a sudden drop and a (reported, but not shown) hysteresis at T_m , as well as a very subtle kink around T_{m2} . Both compounds with $A = \text{Cd}$, and Hg feature an increase of the ZFC magnetic susceptibility with decreasing temperature, and the nearly identical behavior in the field-cooled (FC) magnetic susceptibility.

For $\text{Ca}_2\text{Ru}_2\text{O}_7$ the size of the effective Ru moment could be inferred from a Curie–Weiss fit to the high-temperature magnetic susceptibility, which yields a surprisingly small value of $0.25 - 0.36 \mu_B/\text{Ru}$ [43, 48]. As a comparison, the fully spin-polarized value would be $3.87 \mu_B/\text{Ru}$ using $S = 3/2$ as the spin-quantum number. And even the low-spin state yields $1.73 \mu_B/\text{Ru}$. Moreover, the magnetic susceptibility of $\text{Ca}_2\text{Ru}_2\text{O}_7$ shows a pronounced split between ZFC and FC curve [43], with no upturn in the ZFC case and an almost constant FC measurement. In fact, Taniguchi *et al.* [48] have first ascribed a thermodynamic spin-glass transition to $\text{Ca}_2\text{Ru}_2\text{O}_7$ at T_g by measuring higher-order magnetic susceptibilities.

A spin-glass state is characterized by random, localized magnetic moments with a slow response to external magnetic fields. The muon-spin-rotation (μSR) measurements by Miyazaki *et al.* [47] give further insights to the spin-dynamic properties of $\text{A}_2\text{Ru}_2\text{O}_7$ with $A = \text{Cd}$, Ca , and Hg . They report that around the MIT, a nearly commensurate magnetic order develops in $A = \text{Hg}$, and Cd . But in $\text{Cd}_2\text{Ru}_2\text{O}_7$ below T_m , the presence of a Gaussian distribution at the muon site is interpreted as some randomness of the Ru moments on a regular lattice. For $\text{Ca}_2\text{Ru}_2\text{O}_7$, the same kind of randomness is most pronounced and dubbed *frozen spin liquid*. According to the μSR results, the size of the effective Ru moments is $0.36(7) \mu_B/\text{Ru}$ for $\text{Cd}_2\text{Ru}_2\text{O}_7$ for $T_m < T < T_N$, $0.60 \mu_B/\text{Ru}$ (for $T < T_g$, but $0.35 \mu_B/\text{Ru}$ for $T > T_g$) for $\text{Ca}_2\text{Ru}_2\text{O}_7$, and $0.5(1) \mu_B/\text{Ru}$ for $\text{Hg}_2\text{Ru}_2\text{O}_7$.

Our CMP+SDFT calculations predict that Ψ_4 is the most stable magnetic structure for both, $\text{Ca}_2\text{Ru}_2\text{O}_7$ and $\text{Cd}_2\text{Ru}_2\text{O}_7$, as seen in Figure 2 (a). Note that, all Ru moments in one tetrahedron point outward, which implies that the corner-sharing tetrahedra comprise Ru moments pointing inward. Thus, the magnetic ground state is dubbed AIAO structure. It is separated by only a few meV in total energy from other metastable magnetic configurations obtained by CMP+SDFT. The occurrence of almost degenerate local minima in SDFT is in good agreement with the experimental observation of multiple magnetic transitions.

A list of the magnetic space group (MSPG), Laue group, total energy with respect to the AIAO structure and the predicted size of the Ru moment for all local minima is presented in Table 3. The first column states the dominant BCs, although smaller contributions from additional BCs might further break the symmetry. For the AIAO structure, the MSPG is $\text{Fd}\bar{3}\text{m}'$ and the predicted size of the Ru moments within SDFT is $1.17 \mu_B/\text{Ru}$ for $\text{Ca}_2\text{Ru}_2\text{O}_7$, and $1.07 \mu_B/\text{Ru}$ for $\text{Cd}_2\text{Ru}_2\text{O}_7$. Note that here we refer to the Ru moment along the quantization axis considering

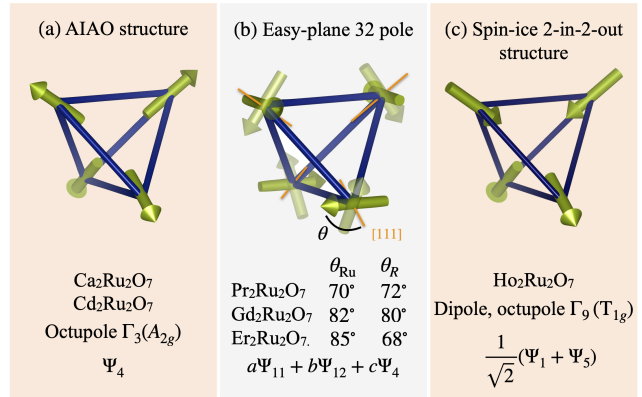


Figure 3. (a) Antiferromagnetic all-in-all-out (AIAO) structure, which corresponds to an octupole with irreducible representation $\Gamma_3(A_{2g})$ and Ψ_4 in Table 2. It is the CMP+SDFT ground state on the Ru sublattice in $\text{Ca}_2\text{Ru}_2\text{O}_7$ and $\text{Cd}_2\text{Ru}_2\text{O}_7$. (b) Easy-plane 32 pole with $\theta = 90^\circ$. A finite contribution of Ψ_4 varies θ . (c) Spin-ice 2-in-2-out structure.

both contributions, the spin and angular-momentum contribution, though the latter is negligible. The predicted value is much smaller than the high-spin state in the ionic limit, i.e., $3 \mu_B$, which implies that the system disobeys Hund's rules as a result of CEF splitting between e'_g and a_{1g} bands due to D_{3d} -site symmetry. Nevertheless, the Ru moments are much larger than the experimentally observed value. This might be due to electronic correlation effects which are not captured in the SDFT-ground-state calculation and will be discussed in Section 3.

The corresponding magnetic crystal information files (MCIFs) for all magnetic structures given in Table 3 are provided in the supplemental material. From Table 3, we see that the SDFT-total-energy landscapes of $\text{Ca}_2\text{Ru}_2\text{O}_7$ and $\text{Cd}_2\text{Ru}_2\text{O}_7$ are similar in the sense that (i) the most stable configuration is the AIAO structure given by Ψ_4 , (ii) Ψ_8 with MSPG $\text{I}4_1'/\text{amd}'(141.555)$ is a local minimum, (iii) magnetic structures dominated by Ψ_5 are local minima, (iv) linear combinations of octupole BCs form other similar local minima. As the AIAO structure has the lowest total energy among all CMP+SDFT calculations and is consistent with the net zero magnetization observed experimentally, it is used in the cRPA and DMFT calculations in Section 3.

2.2. Magnetic structure of $\text{R}_2\text{Ru}_2\text{O}_7$

Let us now consider cubic-pyrochlore rare-earth ruthenates, $\text{R}_2\text{Ru}_2\text{O}_7$. The Ru site hosts a spin $S = 1$ state in the a_{1g} and e'_g bands, and is, consequently, fundamentally different from the Ru site in $\text{A}_2\text{Ru}_2\text{O}_7$ discussed in the previous section. For instance, owing to the integer value of the spin, the system can in principle be in a quantum-paramagnetic phase with

Table 3. CMP+SDFT results for $A_2Ru_2O_7$. The table lists the magnetic space group (MSPG), Laue group, total energy with respect to the AIAO structure (Ψ_4 , highlighted in orange), and predicted size of the magnetic moment along the quantization axis of CMP+SDFT (meta-)stable magnetic structures below 10 meV and with zero net magnetization.

	MSPG	Laue group	meV	μ_B/Ru
Ca₂Ru₂O₇				
Ψ_4	Fd $\bar{3}m'$ (227.131)	m-3m'	0.00	1.17
$\Psi_4\Psi_5\Psi_7\Psi_8\Psi_{10}$	C2'/m'(12.62)	2'/m'	3.96	1.10
Ψ_8	I4 ₁ '/amd'(141.555)	4'/mmm'	5.59	1.12
$\Psi_5\Psi_8$	Fd'd'd'(70.530)	m'm'm	5.99	1.09
$\Psi_4\Psi_{12}$	I4 ₁ '/am'd'(141.554)	4'/mm'm	8.51	1.08
Ψ_5	C2'/c'(15.89)	2'/m'	9.46	1.08
Cd₂Ru₂O₇				
Ψ_4	Fd $\bar{3}m'$ (227.131)	m-3m'	0.00	1.07
Ψ_8	I4 ₁ '/amd'(141.555)	4'/mmm'	2.47	0.93
$\Psi_5\Psi_7\Psi_8\Psi_{10}$	Imm'a'(74.559)	m'm'm	3.17	0.87
$\Psi_5\Psi_6\Psi_7$	R $\bar{3}m'$ (166.101)	-3m'1	5.36	0.77
Ψ_5	I4 ₁ /am'd'(141.557)	4/mm'm'	6.96	0.77

$\mathbf{S} \cdot \hat{z} = S_z = 0$ [50], where \hat{z} is the local [111] direction along the D_{3d} axis. The magnetic ground state of the Ru moments depends on the O–Ru bond length and, thus, on the ionic radius of the rare-earth element $R = \text{Pr, Gd, Ho, and Er}$. Therefore, it depends on R even before considering the d - f -exchange interaction. For the size of the on-site magnetic dipole moment on the Ru site, the ionic limit is given by $2.83 \mu_B/\text{Ru}$ using $S = 1$. Again, the on-site moment for the R site varies depending on the element.

The selected rare-earth elements cover a wide range of different prevalent mechanisms. In particular, for Pr the spin and orbital contributions have a comparable size and combine antiferromagnetically. Thus, the Pr moments are expected to be relatively small and well shielded. The ordering should emerge predominantly under the influence of spin-orbit coupling. On the other hand, for Gd the R - $4f$ bands are half-filled, which results in a vanishing orbital angular momentum and, thus, negligible SOC. Here, d - f -exchange interaction and f - f -exchange interaction could be most important. In $\text{Er}_2\text{Ru}_2\text{O}_7$ and $\text{Ho}_2\text{Ru}_2\text{O}_7$ the spin and orbital contributions add up ferromagnetically which amounts to a large R moment in both cases. In contrast to the case of Pr, these are promising candidate compounds for a dominant dipole-dipole interaction amongst neighboring R sites.

In a broad survey, Ito *et al.* [51] reported the experimental temperature dependence of the specific heat of $R_2\text{Ru}_2\text{O}_7$. In the investigated temperature range, second-order phase transitions associated with the ordering of Ru moments are observed at $T_N \approx 160\text{K}$ for $\text{Pr}_2\text{Ru}_2\text{O}_7$ [52, 51, 53, 54], 114K for $\text{Gd}_2\text{Ru}_2\text{O}_7$ [51, 55], 95K for $\text{Ho}_2\text{Ru}_2\text{O}_7$ [51, 56], and 90K for $\text{Er}_2\text{Ru}_2\text{O}_7$ [51, 57]. In contrast to $A_2\text{Ru}_2\text{O}_7$, for $R_2\text{Ru}_2\text{O}_7$, possible magnetic structures have been recently reported based on neutron scattering using

powder diffraction.

The magnetic structures predicted by CMP+SDFT are summarized in Table 4. The first column lists the most dominant BCs, where Ψ' corresponds to the sublattice of R sites and Ψ to Ru sites. Note that, the CMP basis for the sublattice of both, R sites and Ru sites, is identical and presented in Figure 2 and Table 2. Furthermore, Table 4 lists the MSPG, Laue group, the total energy with respect to the minimum total energy identified within CMP+SDFT (E_{tot} in meV), size of the on-site magnetic dipole moment on the R site and Ru site considering both contributions, the spin and angular-momentum contribution, along the quantization axis, as well as the net magnetization \mathbf{M} per unit formula. In the following, we will discuss the agreement of our numeric results with known experimental observations individually for each compound.

2.2.1. $\text{Pr}_2\text{Ru}_2\text{O}_7$

In particular for $\text{Pr}_2\text{Ru}_2\text{O}_7$, Van Duijn *et al.* [54] determined the magnetic order of the Ru sublattice to be a linear combination of Ψ_{11} and Ψ_{12} of the CMP basis shown in Figure 3 (b) with $c = 0$, i.e., $\theta_{\text{Ru}} = 90^\circ$. Hence, that magnetic structure is a 32 pole in terms of the CMP theory. Regrettably, it is not possible to identify which linear combination of Ψ_{11} and Ψ_{12} is realized based on the powder-diffraction measurement due to the intrinsic ambiguity of the direction of the Ru moments in the (111) plane perpendicular to the local \hat{z} axis, i.e., the [111] direction, when using a powdered sample. In other words, a and b in Figure 3 (b) are unknown. Nevertheless, it is clear that the Ru moments possess AFM order in the local $\hat{x}\hat{y}$ plane, which is distinct from being a quantum paramagnet. The same magnetic structure has been experimentally inferred for the Ru sites of $\text{Y}_2\text{Ru}_2\text{O}_7$ [51], and for the Er sites of $\text{Er}_2\text{Ti}_2\text{O}_7$ [58]. The latter is said to

Table 4. CMP+SDFT results. The table lists the dominant basis configurations Ψ_i (Ψ'_i) for the Ru (R) sublattice, magnetic space group (MSPG), Laue group, total energy E_{tot} with respect to the most stable magnetic structure among all CMP+SDFT calculations, predicted size of the magnetic moment of the Ru and R site along the quantization axis, and the net magnetization per unit formula \mathbf{M} for $R_2\text{Ru}_2\text{O}_7$. For $\text{Gd}_2\text{Ru}_2\text{O}_7$ and $\text{Ho}_2\text{Ru}_2\text{O}_7$ only results with $E_{\text{tot}} \leq 10$ meV are reported. In case of $\text{Gd}_2\text{Ru}_2\text{O}_7$ only (meta-)stable states with zero net magnetization are listed. For $\text{Pr}_2\text{Ru}_2\text{O}_7$ and $\text{Er}_2\text{Ru}_2\text{O}_7$ results with $E_{\text{tot}} \leq 10$ meV and additionally local minima with $E_{\text{tot}} > 10$ meV and zero net magnetization are reported. In orange we highlight the magnetic order we expect is most stable under the constraints known from experimental data as discussed in the main text.

	MSPG	Laue group	meV	μ_B/R	μ_B/Ru	$\mathbf{M}(\mu_B/\text{u.f.})$
$\text{Pr}_2\text{Ru}_2\text{O}_7$						
$\Psi'_1\Psi'_3\Psi'_5\Psi'_7\Psi'_8\Psi'_{10}\Psi_1\Psi_3\Psi_5\Psi_7\Psi_8\Psi_{10}$	Imm'a'(74.559)	m'm'm	0.00	0.80	0.94	6.00
$\Psi'_1\Psi'_2\Psi'_5\Psi'_8\Psi_{11}$	P $\bar{1}$ (2.4)	$\bar{1}$	3.79	0.76	0.95	6.22
$\Psi'_1\Psi'_2\Psi'_3\Psi'_5\Psi_6\Psi_7$	R $\bar{3}m'$ (166.101)	$\bar{3}m'$ 1	5.18	0.74	0.91	6.01
$\Psi'_4\Psi'_{12}\Psi_4\Psi_{12}$	I4 $_1$ '/am'd(141.554)	4'/mm'm	142.19	0.77	1.03	0.00
$\Psi'_{11}\Psi_{11}$	I4 $_1$ /amd(141.551)	4/mmm	151.00	1.01	0.90	0.00
$\Psi'_9\Psi_9$	I4 $_1$ '/amd'(141.555)	4'/mmm'	151.31	1.19	0.88	0.00
$\text{Gd}_2\text{Ru}_2\text{O}_7$						
$\Psi'_4\Psi'_{11}\Psi'_{12}\Psi_4\Psi_{11}\Psi_{12}$	Fddd(70.527)	mmm	0.00	6.86	1.28	0.00
$\Psi'_{11}\Psi'_{12}\Psi_{11}\Psi_{12}$	Fddd(70.527)	mmm	7.69	6.85	1.28	0.00
$\Psi'_{11}\Psi_{11}$	I4 $_1$ /amd(141.551)	4/mmm	7.80	6.84	1.28	0.00
$\text{Ho}_2\text{Ru}_2\text{O}_7$						
$\Psi'_1\Psi'_5(\Psi'_1)\Psi_5$	I4 $_1$ /am'd'(141.557)	4/mm'm'	0.00	9.20	1.29	10.40
$\Psi'_4\Psi_4$	Fd $\bar{3}m'$ (227.131)	m $\bar{3}m'$	2.17	9.26	1.19	0.00
$\text{Er}_2\text{Ru}_2\text{O}_7$						
$\Psi'_3\Psi'_7\Psi_3\Psi_7$	I4 $_1$ /am'd'(141.557)	4/mm'm'	0.00	7.07	1.26	8.54
$\Psi'_1\Psi'_5(\Psi'_1\Psi'_1\Psi'_{12})(\Psi_1\Psi_5)\Psi_{11}\Psi_{12}$	I4 $_1$ /a(88.81)	4/m	0.00	7.07	1.29	8.25
$\Psi'_1\Psi'_5(\Psi'_{12})\Psi_5\Psi_{11}\Psi_{12}$	I4 $_1$ /a(88.81)	4/m	9.14	7.08	1.19	8.81
$\Psi'_{11}\Psi_{11}$	I4 $_1$ /amd(141.551)	4/mmm	38.84	7.57	1.36	0.00
$\Psi'_{11}\Psi_{11}$	I4 $_1$ /amd(141.551)	4/mmm	51.72	7.54	1.30	0.00
$\Psi'_{11}\Psi'_{12}\Psi_8$	Imma(74.554)	mmm	56.76	7.55	1.35	0.00
$\Psi'_4\Psi'_{12}(\Psi_4)\Psi_{12}$	I4 $_1$ '/am'd(141.554)	4'/mm'm	74.08	7.08	1.30	0.00
$\Psi'_4\Psi_4$	Fd $\bar{3}m'$ (227.131)	m $\bar{3}m'$	102.70	6.99	1.14	0.00

feature an accidental continuous rotational symmetry in the $\hat{x}\hat{y}$ plane, which is lifted with an order-by-disorder mechanism [59]. Moreover, Pr is reported not to order down to 100 mK [54] and no more than $0.3\mu_B/\text{Pr}$ may be present without worsening the fit to the experimental data.

The magnetic structure with the lowest total energy in SDFT features BCs with $\Gamma_9(\text{T}_{1g})$ and $\Gamma_9(\text{T}_{2g})$. It has a finite net magnetization in contrast to the experimental observation. The size of the magnetic moments on both sites, Ru and Pr, is comparable to each other in SDFT. Experimentally though, the Ru moments are reported to be $1.48(4)\mu_B/\text{Ru}$ [54], which is a reduction compared to the ionic limit, i.e., $2\mu_B$. We note that the size of Ru moments predicted by SDFT is underestimated compared to the experiment, $0.94\mu_B/\text{Ru} < 1.48(4)\mu_B/\text{Ru}$, but almost within the accuracy of $\pm 0.5\mu_B$ expected for SDFT [13]. On the other hand, the size of Pr moments seems to be overestimated by SDFT, $0.80\mu_B/\text{Pr} > 0.3\mu_B/\text{Pr}$.

In the SDFT calculations, it is mostly the orbital contribution of the Pr- f electrons that introduces a FM tendency towards Ψ'_1 and Ψ'_3 with $\Gamma_9(\text{T}_{1g})$. In contrast, the Ru order is rather biased towards Ψ_5 and Ψ_7 with $\Gamma_9(\text{T}_{1g})$, as well as Ψ_8 and Ψ_{10} with $\Gamma_9(\text{T}_{2g})$.

Note that, both pairs of BCs are octupoles, but with different IRREPs, c.f., Table 2. In Table 4, we see that Pr sites tend to order ferromagnetically with BCs of IRREP $\Gamma_9(\text{T}_{1g})$ also in other low-lying local minima with $E_{\text{tot}} < 10$ meV, which seems to induce octupole order of the same IRREP on the Ru sites. As SDFT overestimates the size of Pr moments and its order influences the order at the Ru sites, we infer that the tendency toward FM order is also overestimated. That is why the low-lying local minima are not reproducing the experimentally observed AFM order.

Nevertheless, the CMP+SDFT scheme is able to find local minima with zero net magnetization at higher total energy. And indeed, the magnetic structures of these AFM local minima are dominated by BCs corresponding to a 32 pole. In particular, the 32 pole highlighted in Table 4 is more stable than other AFM local minima with octupole order. A contribution of Ψ'_4 and Ψ_4 introduces an angle $\theta_{\text{Ru}} \approx 70^\circ$ and $\theta_{\text{Pr}} \approx 72^\circ$ as discussed in more detail for $\text{Gd}_2\text{Ru}_2\text{O}_7$ in the next subsection. We conclude that, we could find an easy-plane 32-pole AFM structure to be among the most stable AFM configurations, which is in good agreement with the experimental result. However, the size of the Pr moments is overestimated within SDFT, which

introduces an FM tendency that is in conflict with the experimental observation.

2.2.2. $Gd_2Ru_2O_7$

For $Gd_2Ru_2O_7$, Mössbauer spectroscopy shows that Ru moments order at $T_N \approx 114K$ [55]. In the magnetic susceptibilities [55, 60], there is a difference between FC and ZFC with a small history-dependent component, which might be explained by a tiny FM contribution due to a canting of the AFM structure. According to Gurgul *et al.* [55], the Ru moments order almost as a 32 pole, but the angle θ_{Ru} enclosed by the Ru moments and the \hat{z} axis is not perfectly 90° as illustrated in Figure 3 (b). Instead, θ_{Ru} is reported to be 72° [55]. This can be accounted for by a linear combination of the BCs of the 32 pole and the octupole Ψ_4 . The resulting magnetic structure is extraordinary in the sense that, it features a combination of multiple IRREPs and this is rather unusual in the context of commonly experimentally determined magnetic structures [13]. Here, the order is a combination of Ψ_4 with $\Gamma_3(A_{2g})$, and Ψ_{11} and Ψ_{12} with $\Gamma_5(E_g)$, c.f., Table 2, Figure 2 (b), (c) and Figure 3 (b). And indeed, a linear combination of the BCs of the 32 poles, Ψ_{11} and Ψ_{12} , and the octupole Ψ_4 is most stable on both, the Gd and Ru sublattices, also within the CMP+SDFT scheme as highlighted in Table 4. The angle $\theta_{Ru} \approx 82^\circ$, which is closer to 90° than the experimental result (72°), but reproduces the overall tendency.

Let us note that, the IRREP of the dipole is $\Gamma_9(T_{1g})$. Therefore, neither Ψ_{11} and Ψ_{12} nor Ψ_4 couples directly to either of the dipole BCs. This stands in contrast to the octupole-magnetic-ground-state structure in Mn_3Sn , where the octupole and dipole have the same IRREP and directly couple, which explains the large anomalous response observed in this compound. That means, the small history dependence of the magnetic susceptibility remains puzzling for $Gd_2Ru_2O_7$. However, besides the AFM local minima listed in Table 2, we identified the staggering number of 16 local minima for $Gd_2Ru_2O_7$ with $E_{tot} < 10meV$. These have a finite net magnetization and are not listed explicitly in Table 2. Let us mention that many of these metastable magnetic structures feature BCs with IRREP $\Gamma_9(T_{1g})$, which easily couple to an applied magnetic field.

At 40K, also the Gd orders as a 32 pole [55], but again no conclusion can be drawn concerning the directions of the Gd moments in the $\hat{x}\hat{y}$ plane based on the experimental data. To our knowledge, it has not been confirmed whether a second-order phase transition can be discerned from the specific heat [61] around 40K. We find that also the Gd sublattices feature a finite angle $\theta_{Gd} \approx 80^\circ$, which was not seen in

the experiment. We emphasize that (i) all three AFM local minima below 10meV feature a 32-pole order, and (ii) the exact linear combination of Ψ_{11} and Ψ_{12} is quasi degenerate as seen by comparing the two metastable magnetic structures around $E_{tot} = 7.7meV$.

The size of the effective Ru moments is reported to be $2.58 \mu_B/Ru$ [61], or $2.12 \mu_B/Ru$ [60], where the former is close to the fully saturated effective Ru moment $2.83 \mu_B$. In contrast, we find the Ru moment along the quantization axis is $1.28 \mu_B/Ru$ within SDFT, which is a reduction by 36% compared to the saturated value of $2 \mu_B/Ru$. For the Gd site, we could not find any report on the size of the Gd moments. Nevertheless, the predicted size of the Gd moments in SDFT seems reasonable when compared to the experimental value for other materials, such as GdB_4 with $7.14 \mu_B/Gd$ [62] and $GdVO_4$ [63] with $7.0 \mu_B/Gd$.

2.2.3. $Ho_2Ru_2O_7$

$Ho_2Ru_2O_7$ has the most intriguing interplay between d and f -electron magnetism and features spin-ice-like states. As shown in Figure 3 (c), a perfect spin-ice structure has two magnetic moments pointing inward along the local \hat{z} axis and two pointing outward in each tetrahedron. It can be obtained by a linear combination of Ψ_1 and Ψ_5 , which both have the same IRREP as seen in Table 2. The Ru moments in $Ho_2Ru_2O_7$ order close to that 2-in-2-out spin-ice structure around 95K [56, 7]. However compared to other known spin ice, e.g., $Ho_2Ti_2O_7$ [6], it behaves as if an external magnetic field of approximately 1 T is present [7]. This has been experimentally confirmed by measurements of the magnetic entropy. Interestingly, the low-temperature specific heat [7] has both (i) a broad feature around 3 K associated with the freezing of magnetic moments, and (ii) a sharp λ anomaly below 2K indicating a second-order phase transition.

At $T_N \approx 1.4K$ [56], the Ho moments order in a spin-ice-like state, but with an additional long-ranged FM order between neighboring tetrahedra within the Ho sublattice due to a small canting of the Ho moments. According to Wiebe *et al.* [56], the Ru moments then abandon the spin-ice-like state and form a nearly collinear FM in the low-temperature regime of 100mK. This fully compensates the FM order of the Ho sublattice and yields zero net magnetization, so that the magnetic structure of $Ho_2Ru_2O_7$ is overall AFM.

In CMP+SDFT, the ground state is a spin-ice-like order on Ho sites, where almost equal contributions from Ψ'_1 and Ψ'_5 emerge. On the Ru sites, we find rather Ψ_5 with little contribution from Ψ_1 . This is the opposite of the experimentally reported behavior, where Ru sites order ferromagnetically to com-

pensate the Ho moments. Therefore, we observe a finite net magnetization in our calculations. Moreover, CMP+SDFT predicts the AIAO structure to be a second almost degenerate metastable magnetic configuration. This hints towards a fickle balance between ferromagnetic and antiferromagnetic interactions on the geometrically frustrated lattice and it might be easily possible to tune the magnetic ground state to obtain the AIAO structure by changing external conditions, e.g., by applying pressure.

The size of the Ru moment is reported as $1.2(2) \mu_B/\text{Ru}$ [56], and the effective Ru moment is reported by different authors as $3.59 \mu_B/\text{Ru}$ [60], and $4.32 \mu_B/\text{Ru}$ [61]. Moreover, the size of the effective Ho moment is reported as $9.60(1) \mu_B/\text{Ho}$ [64] from a Curie-Weiss fit, and the size of the Ho moment in neutron diffraction is $9.29(3) \mu_B/\text{Ho}$ [56]. The size of Ru and Ho moments predicted within SDFT agree well with the values reported by Wiebe *et al.* [56].

2.2.4. $\text{Er}_2\text{Ru}_2\text{O}_7$

For $\text{Er}_2\text{Ru}_2\text{O}_7$, Taira *et al.* [57] suggest that both Ru and Er moments order in a *collinear* AFM structure. At closer inspection it is a linear combination of Ψ_4 , Ψ_{11} and Ψ_{12} . In fact, as these are also powder-diffraction measurements, we assume that the experimental data cannot unambiguously determine the exact linear combination of Ψ_{11} and Ψ_{12} . Instead, the situation seems to be akin to $\text{Gd}_2\text{Ru}_2\text{O}_7$, but with an angle of $\theta_{\text{Ru}} = \theta_{\text{Er}} = 54.74^\circ$. As Siddharthan *et al.* [65] pointed out for rare-earth titanates, the CEF associated with the D_{3d} -site symmetry introduces a strong easy-axis anisotropy along the \hat{z} axis for Ho, but less so for Er. This might cause $\text{Er}_2\text{Ru}_2\text{O}_7$ to attain a AFM 32-pole structure with an easy- $\hat{x}\hat{y}$ -plane AFM configuration rather than a spin-ice-like state, despite its perhaps comparable strength of dipole-dipole interaction as in $\text{Ho}_2\text{Ru}_2\text{O}_7$.

For the Ru sublattice, $T_N \approx 90 \text{ K}$ [57] and the size of the Ru moments is reported as $2.2(2) \mu_B/\text{Ru}$ [61, 57]. Moreover, the Er moments are reported to order at $T_N \approx 10 \text{ K}$ [57, 1], or 5.4 K [61] and their size is reported to be $4.5 \mu_B/\text{Er}$ [57] at 3 K . This is small compared to the value expected in the ionic limit. This reduction has also been observed in other related Er compounds, e.g., $\text{Er}_2\text{Sn}_2\text{O}_7$ [66] and $\text{Er}_2\text{Ti}_2\text{O}_7$ [67].

In our CMP+SDFT calculations, we obtain a degenerate magnetic ground state between a spin-ice-like magnetic structure and a magnetic 32 pole. The former emerges either as combination of Ψ_1 and Ψ_5 , or Ψ_3 and Ψ_7 , while the latter corresponds to any linear combination of Ψ_{11} and Ψ_{12} as shown in Figure 3 (c) and (b), respectively. The BCs in braces are much weaker, and seem to be a result of f - d exchange interaction. We see that the size of the Er moments

is overestimated compared to the experimental value, and that the Er moments tend towards the spin-ice-like configuration. Therefore, we expect that if SDFT would not overestimate the size of the Er moment, the 32-pole order that the Ru moments prefer would prevail.

Below 10 meV , we only find (meta-)stable magnetic structures that have a finite net magnetization. However, when we constrain our analysis to AFM structures, the 32 pole with Ψ'_{11} and Ψ_{11} is indeed the most stable. Curiously, the two most stable AFM structures are both constructed by Ψ'_{11} and Ψ_{11} , but yield a relatively large energy difference of $> 10 \text{ meV}$ owing to the relative orientation of BCs to each other. In particular, parallel alignment with a $\Psi'_{11} \otimes \Psi_{11}$ state has a lower total energy than the $\Psi'_{11} \otimes (-\Psi_{11})$ state. The difference in energy $\Delta E_{\text{tot}} > 10 \text{ meV}$ is a direct measure of the f - d exchange energy.

At about 70 meV , we finally obtain a linear combination of Ψ_4 and Ψ_{12} , which is consistent with the experimental observation up to the angle θ . Experimentally $\theta \approx 54.74^\circ$, but here we find $\theta_{\text{Er}} \approx 68^\circ$ for Er and $\theta_{\text{Ru}} \approx 85^\circ$ for Ru. Additionally, we note that the Ru moment predicted by SDFT is smaller than the one observed experimentally, $1.3 \mu_B/\text{Ru} < 2.2(2) \mu_B/\text{Ru}$ [61, 57]. As a side remark, we mention here that for other isostructural compounds, e.g., $\text{Gd}_2\text{Ru}_2\text{O}_7$ [61, 60], $\text{Tb}_2\text{Ru}_2\text{O}_7$ [61, 60, 68], and $\text{Ho}_2\text{Ru}_2\text{O}_7$ [61, 56, 60] the reported size of the Ru moments vary depending on the authors. Further, investigation on different time scales would thus be beneficial.

2.3. Summary

This closes the discussion about the magnetic structure of both classes of ruthenates, $A_2\text{Ru}_2\text{O}_7$ and $R_2\text{Ru}_2\text{O}_7$. To summarise, our results show that (i) $A_2\text{Ru}_2\text{O}_7$ with $A = \text{Ca}$ and Cd prefers the AIAO structure, (ii) $R_2\text{Ru}_2\text{O}_7$ with $R = \text{Pr}$, Gd , and Er feature an easy-plane 32-pole AFM order with varying angle θ due to a finite contribution from the AIAO structure, (iii) the magnetic ground state of $\text{Ho}_2\text{Ru}_2\text{O}_7$ is spin-ice-like, and (iv) compared to the experimental value within SDFT the size of the magnetic dipole moments per site is (a) well-estimated for Ru and Ho in $\text{Ho}_2\text{Ru}_2\text{O}_7$, (b) overestimated for Ru in $A_2\text{Ru}_2\text{O}_7$, as well as for Pr and Er, and (c) underestimated for Ru in $R_2\text{Ru}_2\text{O}_7$ with $R = \text{Pr}$ and Er , while for the $\text{Gd}_2\text{Ru}_2\text{O}_7$ the experimental data to make a direct comparison has not been reported. Albeit the main focus in the next section is on electronic properties, the size of the moments is also briefly discussed.

3. Electronic properties

From experimental observations, it is clear that electronic correlations play an important role in $A_2\text{Ru}_2\text{O}_7$ and $R_2\text{Ru}_2\text{O}_7$. Particularly, the resistivity shows metallic behavior for $\text{Ca}_2\text{Ru}_2\text{O}_7$ and insulating behavior for $\text{Pr}_2\text{Ru}_2\text{O}_7$ [69, 4]. This tendency can be confirmed by means of the optical conductivity, which shows a gap for $\text{Pr}_2\text{Ru}_2\text{O}_7$ and no gap for $\text{Ca}_2\text{Ru}_2\text{O}_7$ up to experimental uncertainty. Hence, despite the success in reproducing the experimental magnetic structure based on CMP+SDFT in the previous section, above observations call for a careful treatment of electronic correlations beyond SDFT.

Here, we focus on the $\text{Ru-}t_{2g}$ manifold that forms the conduction bands in SDFT and governs the electronic properties of $A_2\text{Ru}_2\text{O}_7$ and $R_2\text{Ru}_2\text{O}_7$. Among the discussed compounds, we pick two representative ones: $\text{Ca}_2\text{Ru}_2\text{O}_7$ and $\text{Pr}_2\text{Ru}_2\text{O}_7$. The main motivation is given by recent works by Kaneko *et al.* [69, 4], where $(\text{Ca}_{1-x}\text{Pr}_x)_2\text{Ru}_2\text{O}_7$ has been investigated and the doping parameter x could be continuously tuned. Yet, let us emphasize at this point that $\text{Ca}_2\text{Ru}_2\text{O}_7$ and $\text{Cd}_2\text{Ru}_2\text{O}_7$ have demonstrated a great similarity in the SDFT-total-energy landscape discussed in the previous section. Furthermore, $\text{Pr}_2\text{Ru}_2\text{O}_7$ is the most natural choice among the rare-earth ruthenates, when focusing on the $\text{Ru-}t_{2g}$ bands as we do here. That is because Pr moments do not order and it is thus well-justified to neglect strong d - f exchange interaction when considering the electronic properties.

Finally, before constructing a low-energy effective model and solving it within DMFT, let us recall that the central difference between $\text{Ca}_2\text{Ru}_2\text{O}_7$ and $\text{Pr}_2\text{Ru}_2\text{O}_7$ is that the $\text{Ru-}t_{2g}$ bands are occupied by 3 and 4 electrons, respectively. It is noteworthy, that experimentally the $\text{Ru-}t_{2g}$ bands in $\text{Pr}_2\text{Ru}_2\text{O}_7$ are more strongly correlated than the half-filled case of $\text{Ca}_2\text{Ru}_2\text{O}_7$. This is unexpected for correlated, multiorbital systems [8]. The underlying mechanisms that introduces this counterintuitive tendency are elucidated in the following.

3.1. Low-energy effective models for $\text{Ca}_2\text{Ru}_2\text{O}_7$ and $\text{Pr}_2\text{Ru}_2\text{O}_7$

To derive the low-energy effective models for the $\text{Ru-}t_{2g}$ manifold for $\text{Ca}_2\text{Ru}_2\text{O}_7$ and $\text{Pr}_2\text{Ru}_2\text{O}_7$, we employ a combination of the maximally-localized Wannier functions [70, 71] and the cRPA method [12]. The construction of Wannier functions and the cRPA calculations are performed with an open-source package RESPACK [72, 73]. In the cRPA calculations, RESPACK employs the band disentanglement scheme proposed in Ref. [74].

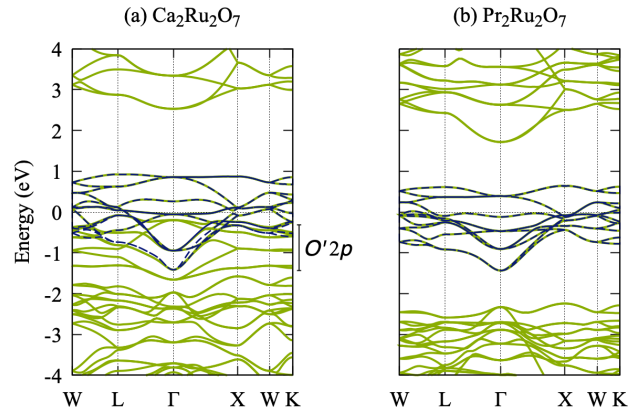


Figure 4. Band structure for (a) $\text{Ca}_2\text{Ru}_2\text{O}_7$ and (b) $\text{Pr}_2\text{Ru}_2\text{O}_7$. The green lines are based on a DFT calculation, while the blue dashed lines are based on maximally-localized Wannier functions for the $\text{Ru-}t_{2g}$ orbitals. For $\text{Ca}_2\text{Ru}_2\text{O}_7$, the entangled $\text{O}'\text{-}2p$ bands, c.f., Table 1, introduce additional screening.

We first perform the DFT-band-structure calculations for $\text{Ca}_2\text{Ru}_2\text{O}_7$ and $\text{Pr}_2\text{Ru}_2\text{O}_7$ using QUANTUM ESPRESSO [75] ¶. The result is shown in Figure 4 as green lines. The structures for $\text{Ca}_2\text{Ru}_2\text{O}_7$ and $\text{Pr}_2\text{Ru}_2\text{O}_7$ are taken from Refs. [43] and [76], respectively. The optimized norm-preserving Vanderbilt pseudopotentials [77] with the PBE (Perdew-Burke-Ernzerhof) exchange-correlation functional [78] are downloaded from PseudoDojo [79] and employed in the DFT calculations. We use $9 \times 9 \times 9$ \mathbf{k} mesh, and the energy cutoff is set to 100 Ry for the wavefunction and 400 Ry for the electron-charge density.

The maximally localized Wannier functions [70, 71] are constructed with the projections of $\text{Ru-}a_{1g}$ and e'_g orbitals. The resulting bands are shown in Figure 4 as dashed blue lines around the Fermi energy set to 0 eV. For $\text{Ca}_2\text{Ru}_2\text{O}_7$, the $\text{Ru-}t_{2g}$ bands are overlapping with the $\text{O}'\text{-}2p$ bands, where O' refers to the oxygen atom at Wyckoff position $8b$ as defined in Table 1 and illustrated Figure 1 (a) and (c). That is why we employ both the outer and inner windows whose energy ranges are $[-1.45 \text{ eV} : 1.5 \text{ eV}]$ and $[-0.18 \text{ eV} : 1.5 \text{ eV}]$, respectively. For $\text{Pr}_2\text{Ru}_2\text{O}_7$, the $\text{Ru-}t_{2g}$ bands are isolated from the other bands, and the Wannier functions are constructed from the energy range of $[-1.5 \text{ eV} : 1.5 \text{ eV}]$. For the constructed Wannier orbitals, we calculate the effective interaction parameters using the cRPA method. The polarization function is calculated using 200 bands with the energy cutoff of 10 Ry.

The derived Hubbard interaction parameters are

¶ The reason to use a different *ab-initio* code here is that RESPACK provides a convenient interface to QUANTUM ESPRESSO. The DFT results between VASP and QUANTUM ESPRESSO show no discernible difference, which serves as an additional cross-validation for our numerical results.

Table 5. cRPA results for the Hubbard interaction U_{cRPA} for $\text{Ca}_2\text{Ru}_2\text{O}_7$ and $\text{Pr}_2\text{Ru}_2\text{O}_7$. To see the effect of the screening, we also show the results of bare interaction U_{bare} .

		U_{bare} (eV)	U_{cRPA} (eV)	$U_{\text{cRPA}}/U_{\text{bare}}$
$\text{Ca}_2\text{Ru}_2\text{O}_7$	a_{1g}	9.42	1.10	0.12
	e'_g	9.82	1.16	0.12
$\text{Pr}_2\text{Ru}_2\text{O}_7$	a_{1g}	11.33	2.36	0.21
	e'_g	11.48	2.42	0.21

listed in Table 5. Interestingly, we see a drastic change in U parameters between $\text{Ca}_2\text{Ru}_2\text{O}_7$ and $\text{Pr}_2\text{Ru}_2\text{O}_7$: Whereas the on-site U is comparable to the bandwidth in the case of $\text{Pr}_2\text{Ru}_2\text{O}_7$, in the case of $\text{Ca}_2\text{Ru}_2\text{O}_7$, the U value is much smaller. This gives rise to a significant difference in the electronic correlation as discussed below in Section 3.2.

The large difference in the U value can be ascribed to the spatial spread of the Wannier orbitals and the strength of the screening. In $\text{Ca}_2\text{Ru}_2\text{O}_7$, the nominal valence of the Ru cations is $5+$, and the energy of Ru- t_{2g} orbitals is lowered compared to the Pr compound with Ru^{4+} cations due to the stronger attractive potential from the nuclei. This draws the energy levels of the Ru- t_{2g} and O- $2p$ orbitals closer together. As a result, the hybridization between Ru- t_{2g} and O- $2p$ orbitals becomes larger, and the Wannier functions become more delocalized in space. The difference of the spatial spread of the Wannier orbitals is reflected in the bare U value (U_{bare}) listed in Table 5: We indeed see that the bare U values for $\text{Ca}_2\text{Ru}_2\text{O}_7$ are smaller than those of $\text{Pr}_2\text{Ru}_2\text{O}_7$.

The difference in the screening results in an even more considerable difference in the U values than the difference of the spatial spread of the Wannier orbitals. As we see in Table 5, in $\text{Ca}_2\text{Ru}_2\text{O}_7$, the screening effect is much stronger than that of $\text{Pr}_2\text{Ru}_2\text{O}_7$, and U_{cRPA} is about 10 times smaller than U_{bare} . This is because the energy levels of O- $2p$ and O'- $2p$ bands move closer to the Fermi level. In particular, the O'- $2p$ bands overlap with the Ru- t_{2g} manifold in $\text{Ca}_2\text{Ru}_2\text{O}_7$ and lie very close to the Fermi level, which yields a large contribution to the screening. That is due to the smaller energy that appears in the denominator of expression for the polarization function.

Because the strength of the screening is sensitive to the energy level of the O' bands in $\text{Ca}_2\text{Ru}_2\text{O}_7$, we may be able to change the U value significantly by controlling the position of the O'- $2p$ bands by, e.g., applying external pressure. Motivated by this expectation, we perform the cRPA calculations for $\text{Ca}_2\text{Ru}_2\text{O}_7$ with different lattice constants (internal coordinates are fixed). When the lattice constant is 4% (2%) smaller, the U_{cRPA} values become 1.41 (1.24) eV and 1.45 (1.28) eV for Ru- a_{1g} and Ru- e'_g orbitals,

respectively. We observe an increase as large as about several tens percent in the value of U by external pressure. The result is of great interest because, in $\text{Ca}_2\text{Ru}_2\text{O}_7$, applying pressure might make the compound more strongly correlated as a result of the drastic increase in U , which thus can get larger than the increase in the bandwidth. This is in stark contrast with a common belief that the external pressure weakens the electronic correlation. That is based on the fact that in usual materials, the bandwidth increases, whereas the U value gets less affected. Such an interesting effect would also be seen in other Ru^{5+} compounds, i.e., $\text{A}_2\text{Ru}_2\text{O}_7$, such as $\text{Cd}_2\text{Ru}_2\text{O}_7$. Indeed, there is an experimental report that applying chemical or external pressure unexpectedly induces a MIT in the Cd compound [5].

3.2. DMFT results

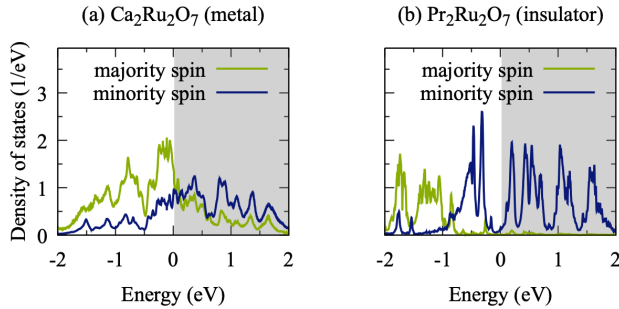
Based on the maximally-localized Wannier functions and cRPA results discussed in the previous subsection, we construct low-energy effective models for $\text{Ca}_2\text{Ru}_2\text{O}_7$ and $\text{Pr}_2\text{Ru}_2\text{O}_7$, and solve them within the DMFT. The DMFT impurity problem is solved employing the finite-temperature extension [80, 81] of the exact diagonalization method [82], where the dynamical mean field is represented by 9 bath sites.

For $\text{Ca}_2\text{Ru}_2\text{O}_7$, although the zero-temperature magnetic structure is controversial in experiments, our CMP+SDFT results suggest that the AIAO structure shown in Figure 2 is the magnetic ground state. Therefore, we assume that the AFM exchange interaction between Ru sites is of the AIAO type in the DMFT calculation. This allows to copy the self-energy matrix with respect to spin and orbital degrees of freedom, that is obtained by solving the impurity problem at one Ru site, to the other three Ru sites in the crystallographic unit cell by taking into account the appropriate rotation in the spin-orbital space. Generally, this setup permits to converge to either a spin-polarized AFM AIAO state or non-spin-polarized state.

In the low temperature regime at $T \approx 50$ K, we indeed converge to the AFM AIAO state, where both Ru- a_{1g} and Ru- e'_g orbitals are nearly half-filled with an occupancy of approximately 1 and 2 electrons,

Table 6. Orbital occupancy at a Ru site in the AIAO state calculated within DMFT at $T \approx 50$ K. Note that the e'_g orbitals are doubly degenerate.

	orbital	majority spin	minority spin	total
$\text{Ca}_2\text{Ru}_2\text{O}_7$	Ru- a_{1g}	0.78	0.36	1.14
	Ru- e'_g	1.25	0.60	1.85
$\text{Pr}_2\text{Ru}_2\text{O}_7$	Ru- a_{1g}	1.00	0.99	1.99
	Ru- e'_g	1.94	0.08	2.01

**Figure 5.** Local density of states at one Ru site, calculated with the DMFT for the low-energy effective models for (a) $\text{Ca}_2\text{Ru}_2\text{O}_7$, and (b) $\text{Pr}_2\text{Ru}_2\text{O}_7$.

respectively. The exact values are presented in Table 6. Obviously, the occupancies sum up to 3 electrons within the Ru- t_{2g} manifold. At each Ru site, there is a majority spin and a minority spin, which refers to the local spin-up and spin-down state according to the AIAO structure. From Table 6, we see that each orbital at a Ru site is not fully spin-polarized but yields an on-site magnetic moment of $1.07 \mu_B/\text{Ru}$, which will be discussed below.

Figure 5 (a) shows the local density of states at the Ru site in $\text{Ca}_2\text{Ru}_2\text{O}_7$. The accumulation of majority-spin states below the Fermi energy at 0 eV yields a large spin-polarization. Additionally, we see that no gap appears at the Fermi level and the DMFT solution is indeed metallic. This is due to the relatively small value of U , which is a consequence of the substantial screening by the O' - $2p$ bands. Overall, this is consistent with the observed bad-metallic behavior in the experimentally measured resistivity [4].

On the other hand, following the same procedure for $\text{Pr}_2\text{Ru}_2\text{O}_7$ yields an insulating DMFT solution as seen in Figure 5 (b). Note that also here we assume the AFM AIAO state, which is justified by the fact that the insulating behavior is expected to be independent of the choice of the magnetic structure as it appears in all compounds of $R_2\text{Ru}_2\text{O}_7$. Additionally, we see in SDFT that the AIAO state is metastable so that we can obtain a converged solution. Nevertheless, as discussed in Section 2 the ground-state magnetic order is a 32-pole with small contributions from the AIAO

structure. By means of our DMFT results, the size of the band gap can be estimated to be about 0.2 eV. This agrees well with the reported value based on the optical-conductivity measurements [69], i.e., 0.25 eV. The formation of the band gap in $\text{Pr}_2\text{Ru}_2\text{O}_7$ is ascribed to the large value of the screened interactions U_{cRPA} compared to the more substantially screened, and thus smaller, value of U_{cRPA} in $\text{Ca}_2\text{Ru}_2\text{O}_7$, c.f., Table 5. Thus, the strong electronic correlation in $\text{Pr}_2\text{Ru}_2\text{O}_7$ drives it into an insulating state, while the stronger screening in $\text{Ca}_2\text{Ru}_2\text{O}_7$ allows the metallic state to prevail.

From Table 6, one can see that the Ru- a_{1g} orbital is basically fully occupied in $\text{Pr}_2\text{Ru}_2\text{O}_7$, while the Ru- e'_g orbitals are half-filled. Therefore, the spin-polarization emerges on the latter, in contrast to the case of $\text{Ca}_2\text{Ru}_2\text{O}_7$ where all Ru- t_{2g} bands contribute. Let us recall that, for $\text{Ca}_2\text{Ru}_2\text{O}_7$ the effective Ru moment is reported as $0.60 \mu_B/\text{Ru}$ based on μSR results [47], where also glasslike randomness was detected. The Ru moment defined in SDFT is $1.17 \mu_B/\text{Ru}$, as discussed in Section 2.1, which is clearly larger than the experimental value. Within DMFT we obtain $1.07 \mu_B/\text{Ru}$ for the Ru moment. That is a minor reduction and is still larger than the experimental value. For $\text{Pr}_2\text{Ru}_2\text{O}_7$, the the Ru moment is (i) $1.48(4) \mu_B/\text{Ru}$ in experiment [54], (ii) $0.94 \mu_B/\text{Ru}$ in SDFT, and (iii) $1.87 \mu_B/\text{Ru}$ in DMFT. In both cases, we see that the inclusion of local quantum fluctuations within DMFT improves upon the predicted magnetic moment although the deviation from the experimental value cannot be fully amended. That might point towards more intriguing mechanisms based on spin-dynamic effects and magnetic frustration that are not yet taken into account on the level of the present low-energy effective model solved within DMFT.

4. Conclusion

We have described the magnetic structure and electronic properties of $R_2\text{Ru}_2\text{O}_7$ with $R^{3+} = \text{Pr}, \text{Gd}, \text{Ho}, \text{and Er}$, as well as $A_2\text{Ru}_2\text{O}_7$ with nonmagnetic $A^{2+} = \text{Ca}, \text{and Cd}$ from first-principles. That is, with $\text{Er}_2\text{Ru}_2\text{O}_7$, we tackled the most challenging compound that was included

in the data set of the high-throughput calculation in which some of the present authors introduced the CMP+SDFT prediction scheme [13]. Initially, it seemed CMP+SDFT fails to treat $\text{Er}_2\text{Ru}_2\text{O}_7$ well, and by extension we expected that $R_2\text{Ru}_2\text{O}_7$ is generally not well-described within this scheme. Motivated by the interest of Kaneko *et al.* [69, 4] in $(\text{Ca}_{1-x}\text{Pr}_x)_2\text{Ru}_2\text{O}_7$, we once again faced this class of materials. To our great surprise and delight, we found good agreement of our numeric results and the available experimental data at closer inspection.

For the magnetic ground state, we have demonstrated that the discussion of magnetic structures featured in cubic-pyrochlore ruthenates greatly benefits from the classification in terms of the CMP theory. Firstly, the easy-plane AFM structure realized in $R_2\text{Ru}_2\text{O}_7$ with $R = \text{Pr}$, Gd , and Er corresponds to a 32 pole. Due to the easy plane and ambiguity in the powder-diffraction measurements, there is a particular need to take care when comparing the numerical and experimental results, which is done within the scope of this work. Secondly, the spin-ice structure is a linear combination of a dipole and octupole that both have T_{1g} symmetry. And lastly, the AIAO is prominently classified as the A_{2g} octupole. The CMP+SDFT scheme successfully leads to the identification of key tendencies when varying A and R elements. This is most significantly shown by the fact that, the magnetic ground state of $\text{Ho}_2\text{Ru}_2\text{O}_7$ is spin-ice-like, while the other rare-earth ruthenates— $R_2\text{Ru}_2\text{O}_7$ with $R = \text{Pr}$, Gd , and Er —feature an easy-plane 32-pole AFM order. Also, our data shows that $\text{A}_2\text{Ru}_2\text{O}_7$ with $A = \text{Ca}$ and Cd prefers the AIAO structure.

For the electronic properties, band-structure and cRPA calculations reveal that the relative energy of $O-2p$ and $O'-2p$ bands with respect to the $\text{Ru}-t_{2g}$ bands controls the strength of electronic correlation. Building upon that, we constructed a low-energy effective model that can qualitatively and quantitatively account for the metallic state in $\text{Ca}_2\text{Ru}_2\text{O}_7$ and the Mott-insulating state in $\text{Pr}_2\text{Ru}_2\text{O}_7$. In particular, the band gap in $\text{Pr}_2\text{Ru}_2\text{O}_7$ is in good agreement with the optical-conductivity measurement.

Regarding the size of the on-site magnetic moment, regrettably, it cannot be reliably reproduced. There are varying tendencies towards either over- or underestimation within SDFT depending on the magnetic site. The DMFT calculations based on our low-energy effective model for $\text{Ca}_2\text{Ru}_2\text{O}_7$ and $\text{Pr}_2\text{Ru}_2\text{O}_7$ slightly improve the agreement of the experimental value compared to the SDFT result. As this does not fully correct the numerical values, we suspect that spin-dynamic effects and magnetic frustration that are beyond the scope here actually play

a significant role.

Looking forward, there are still plenty of intriguing mysteries to be solved for pyrochlore ruthenates: Firstly, it could be interesting to investigate the spin dynamics of these systems. This is not only promising with respect to the predicted size of the on-site magnetic moment, but also to elucidate the experimental evidence of spin glass behavior in $\text{Ca}_2\text{Ru}_2\text{O}_7$ [48, 47] and $\text{Cd}_2\text{Ru}_2\text{O}_7$ [47]. Next, it will be interesting to fully account for doping in our calculations in order to catch up with the experimental capability. In this context, there are new magnetic states, complex doping-dependency of the resistivity and a MIT to explore. For instance, $(\text{Ca}_{1-x}\text{Pr}_x)_2\text{Ru}_2\text{O}_7$ with small x seems to have a FM ground state. Then, the magnetic order in different temperature regimes deserves a closer look. In fact, for $\text{Ho}_2\text{Ru}_2\text{O}_7$ the magnetic order on the Ru site shifts from a spin-ice-like structure to an almost collinear FM at low temperatures where the Ho site orders as a spin-ice-like structure with a small FM canting that aligns AFM with the Ru sublattice. To our knowledge, the experimental high-temperature magnetic structure of other cubic-pyrochlore ruthenates has not been reported and may reveal further surprising shifts. And lastly, it will be interesting to investigate in more detail the relationship between our findings with regards to the $O'-2p$ bands and the experimentally observed pressure-induced MIT in $\text{Cd}_2\text{Ru}_2\text{O}_7$.

Acknowledgments

We thank Yoshinori Tokura, Kentaro Ueda, and Ryoma Kaneko for directing our attention to these materials and for valuable discussions. This work was supported by JSPS KAKENHI (Grant No. JP19H02594 19H05825, 21H04437, 21H04990, 20K14423, and 21H01041) and “Program for Promoting Researches on the Supercomputer Fugaku” (Project ID: hp210163) from MEXT.

References

- [1] Gardner J S, Gingras M J and Greedan J E 2010 *Reviews of Modern Physics* **82** 53
- [2] Rau J G and Gingras M J 2019 *Annual Review of Condensed Matter Physics* **10** 357–386
- [3] Ueda K, Fukuda H, Kaneko R, Fujioka J and Tokura Y 2020 *Physical Review B* **102** 245131
- [4] Kaneko R, Ueda K, Sakai S, Nomura Y, Huebsch M T, Arita R and Tokura Y 2021 *Physical Review B* **103** L201111
- [5] Jiao Y Y, Sun J P, Shahi P, Cui Q, Yu X H, Uwatoko Y, Wang B S, Alonso J A, Weng H M and Cheng J G 2018 *Phys. Rev. B* **98**(7) 075118 URL <https://link.aps.org/doi/10.1103/PhysRevB.98.075118>
- [6] Bramwell S T and Gingras M J 2001 *Science* **294** 1495–1501
- [7] Gardner J, Cornelius A, Chang L J, Prager M, Brückel T and Ehlers G 2005 *Journal of Physics: Condensed Matter* **17** 7089

- [8] Georges A, Medici L d and Mravlje J 2013 *Annu. Rev. Condens. Matter Phys.* **4** 137–178
- [9] Takeshita N, Terakura C, Tokura Y, Yamamoto A and Takagi H 2007 *Journal of the Physical Society of Japan* **76** 063707–063707
- [10] Kübler J 2017 *Theory of itinerant electron magnetism* vol 106 (Oxford University Press)
- [11] Georges A, Kotliar G, Krauth W and Rozenberg M J 1996 *Reviews of Modern Physics* **68** 13
- [12] Aryasetiawan F, Imada M, Georges A, Kotliar G, Biermann S and Lichtenstein A I 2004 *Phys. Rev. B* **70**(19) 195104 URL <https://link.aps.org/doi/10.1103/PhysRevB.70.195104>
- [13] Huebsch M T, Nomoto T, Suzuki M T and Arita R 2021 *Physical Review X* **11** 011031
- [14] Sugano S 2012 *Multiplets of transition-metal ions in crystals* (Elsevier)
- [15] Subramanian M, Aravamudan G and Rao G S 1983 *Progress in Solid State Chemistry* **15** 55–143
- [16] Harris M J, Bramwell S, McMorro D, Zeiske T and Godfrey K 1997 *Physical Review Letters* **79** 2554
- [17] Bramwell S, Harris M, Den Hertog B, Gingras M, Gardner J, McMorro D, Wildes A, Cornelius A, Champion J, Melko R *et al.* 2001 *Physical Review Letters* **87** 047205
- [18] Kusunose H 2008 *Journal of the Physical Society of Japan* **77** 064710–064710
- [19] Santini P, Carretta S, Amoretti G, Caciuffo R, Magnani N and Lander G H 2009 *Reviews of Modern Physics* **81** 807
- [20] Hayami S, Yatsushiro M, Yanagi Y and Kusunose H 2018 *Physical Review B* **98** 165110
- [21] Hayami S and Kusunose H 2018 *Journal of the Physical Society of Japan* **87** 033709
- [22] Dubovik V and Tugushev V 1990 *Physics reports* **187** 145–202
- [23] Hayami S, Kusunose H and Motome Y 2016 *Journal of Physics: Condensed Matter* **28** 395601
- [24] Suzuki M T, Koretsune T, Ochi M and Arita R 2017 *Physical Review B* **95** 094406
- [25] Suzuki M T, Ikeda H and Oppeneer P M 2018 *Journal of the Physical Society of Japan* **87** 041008
- [26] Huyen V T N, Suzuki M T, Yamauchi K and Oguchi T 2019 *Physical Review B* **100** 094426
- [27] Hayami S and Kusunose H 2021 *Physical Review B* **103** L180407
- [28] Suzuki M T, Nomoto T, Arita R, Yanagi Y, Hayami S and Kusunose H 2019 *Physical Review B* **99** 174407
- [29] Landau L D and Lifshitz E M 2013 *Course of theoretical physics* (Elsevier)
- [30] Rietveld H M 1969 *Journal of applied Crystallography* **2** 65–71
- [31] Hovestreydt E, Aroyo M, Sattler S and Wondratschek H 1992 *Journal of Applied Crystallography* **25** 544–544
- [32] Wills A 2000 *Physica B: Condensed Matter* **276** 680–681
- [33] Sikora W, Białas F and Pytlík L 2004 *Journal of Applied Crystallography* **37** 1015–1019
- [34] Stokes H T, Hatch D M, Campbell B J and Tanner D E 2006 *Journal of Applied Crystallography* **39** 607–614
- [35] Aroyo M I, Perez-Mato J, Orobengoa D, Tasci E, de la Flor G and Kirov A 2011 *Bulg. Chem. Commun* **43** 183–197
- [36] Wills A 2015 Indexing magnetic structures and crystallographic distortions from powder diffraction: Brillouin zone indexing *Eleventh European Powder Diffraction Conference* (Oldenbourg Wissenschaftsverlag) pp 39–44
- [37] Kresse G and Hafner J 1993 *Physical review B* **47** 558
- [38] Kresse G and Hafner J 1994 *Physical Review B* **49** 14251
- [39] Hobbs D and Hafner J 2001 *Journal of Physics: Condensed Matter* **13** L681
- [40] Steiner S, Khmelevskiy S, Marsmann M and Kresse G 2016 *Physical review B* **93** 224425
- [41] <https://icsd.fiz-karlsruhe.de>
- [42] Wang R and Sleight A 1998 *Materials Research Bulletin* **33**
- [43] Munenaka T and Sato H 2006 *Journal of the Physical Society of Japan* **75** 103801
- [44] Yamamoto A, Sharma P A, Okamoto Y, Nakao A, Katori H A, Niitaka S, Hashizume D and Takagi H 2007 *journal of the physical society of japan* **76** 043703–043703
- [45] Klein W, Kremer R K and Jansen M 2007 *Journal of Materials Chemistry* **17** 1356–1360
- [46] van Duijn J, Ruiz-Bustos R and Daoud-Aladine A 2012 *Physical Review B* **86** 214111
- [47] Miyazaki M, Kadono R, Satoh K, Hiraishi M, Takeshita S, Koda A, Yamamoto A and Takagi H 2010 *Physical Review B* **82** 094413
- [48] Taniguchi T, Munenaka T and Sato H 2009 Spin glass behavior in metallic pyrochlore ruthenate $\text{Ca}_2\text{Ru}_2\text{O}_7$ *Journal of Physics: Conference Series* vol 145 (IOP Publishing) p 012017
- [49] Krimmel A, Günther A, Kraetschmer W, Dekinger H, Büttgen N, Loidl A, Ebbinghaus S G, Scheidt E W and Scherer W 2008 *Physical Review B* **78** 165126
- [50] Li F Y and Chen G 2018 *Physical Review B* **98** 045109
- [51] Ito M, Yasui Y, Kanada M, Harashina H, Yoshii S, Murata K, Sato M, Okumura H and Kakurai K 2001 *Journal of Physics and Chemistry of Solids* **62** 337–341
- [52] Taira N, Wakeshima M and Hinatsu Y 1999 *Journal of Physics: Condensed Matter* **11** 6983
- [53] Tachibana M, Kohama Y, Atake T and Takayama-Muromachi E 2007 *Journal of applied physics* **101** 09D502
- [54] Van Duijn J, Kim K, Hur N, Ruiz-Bustos R, Adroja D, Bridges F, Daoud-Aladine A, Fernandez-Alonso F, Wen J, Kearney V *et al.* 2017 *Physical Review B* **96** 094409
- [55] Gurgul J, Rams M, Swiatkowska Z, Kmiec R and Tomala K 2007 *Physical Review B* **75** 064426
- [56] Wiebe C, Gardner J, Kim S J, Luke G, Wills A, Gaulin B, Greedan J, Swainson I, Qiu Y and Jones C 2004 *Physical review letters* **93** 076403
- [57] Taira N, Wakeshima M, Hinatsu Y, Tobo A and Ohoyama K 2003 *Journal of Solid State Chemistry* **176** 165–169
- [58] Poole A, Wills A and Lelievre-Berna E 2007 *Journal of Physics: Condensed Matter* **19** 452201
- [59] Savary L, Ross K A, Gaulin B D, Ruff J P and Balents L 2012 *Physical review letters* **109** 167201
- [60] Yao L, Wang D, Peng W, Hu W, Yuan H and Feng S 2011 *Science China Chemistry* **54** 941–946
- [61] Taira N, Wakeshima M and Hinatsu Y 2002 *Journal of Materials Chemistry* **12** 1475–1479
- [62] Blanco J A, Brown P J, Stunault A, Katsumata K, Iga F and Michimura S 2006 *Physical Review B* **73** 212411 ISSN 1098-0121 URL <https://link.aps.org/doi/10.1103/PhysRevB.73.212411>
- [63] Palacios E, Evangelisti M, Sáez-Puche R, Dos Santos-García A J, Fernández-Martínez F, Cascales C, Castro M, Burriel R, Fabelo O and Rodríguez-Velamazán J A 2018 *Physical Review B* **97** 214401 ISSN 2469-9950 URL <https://link.aps.org/doi/10.1103/PhysRevB.97.214401>
- [64] Bansal C, Kawanaka H, Bando H and Nishihara Y 2003 *Physica B: Condensed Matter* **329** 1034–1035
- [65] Siddharthan R, Shastry B, Ramirez A, Hayashi A, Cava R and Rosenkranz S 1999 *Physical review letters* **83** 1854
- [66] Matsuhira K, Hinatsu Y, Tenya K, Amitsuka H and Sakakibara T 2002 *Journal of the Physical Society of Japan* **71** 1576–1582
- [67] Bramwell S, Field M, Harris M and Parkin I 2000 *Journal of Physics: Condensed Matter* **12** 483
- [68] Xiao D, Chang M C and Niu Q 2010 *Reviews of modern physics* **82** 1959
- [69] Kaneko R, Ueda K, Terakura C and Tokura Y 2020 *Phys. Rev. B* **102**(4) 041114 URL <https://link.aps.org/doi/>

- 10.1103/PhysRevB.102.041114
- [70] Marzari N and Vanderbilt D 1997 *Phys. Rev. B* **56**(20) 12847–12865 URL <https://link.aps.org/doi/10.1103/PhysRevB.56.12847>
 - [71] Souza I, Marzari N and Vanderbilt D 2001 *Phys. Rev. B* **65**(3) 035109 URL <https://link.aps.org/doi/10.1103/PhysRevB.65.035109>
 - [72] Nakamura K, Yoshimoto Y, Nomura Y, Tadano T, Kawamura M, Kosugi T, Yoshimi K, Misawa T and Motoyama Y 2021 *Computer Physics Communications* **261** 107781
 - [73] <https://sites.google.com/view/kazuma7k6r>
 - [74] Şaşıoğlu E, Friedrich C and Blügel S 2011 *Phys. Rev. B* **83**(12) 121101 URL <https://link.aps.org/doi/10.1103/PhysRevB.83.121101>
 - [75] Giannozzi P, Andreussi O, Brumme T, Bunau O, Nardelli M B, Calandra M, Car R, Cavazzoni C, Ceresoli D, Cococcioni M, Colonna N, Carnimeo I, Corso A D, de Gironcoli S, Delugas P, Jr R A D, Ferretti A, Floris A, Fratesi G, Fugallo G, Gebauer R, Gerstmann U, Giustino F, Gorni T, Jia J, Kawamura M, Ko H Y, Kokalj A, Kucukbenli E, Lazzeri M, Marsili M, Marzari N, Mauri F, Nguyen N L, Nguyen H V, de-la Roza A O, Paulatto L, Ponce S, Rocca D, Sabatini R, Santra B, Schlipf M, Seitsonen A P, Smogunov A, Timrov I, Thonhauser T, Umari P, Vast N, Wu X and Baroni S 2017 *Journal of Physics: Condensed Matter* **29** 465901 URL <http://stacks.iop.org/0953-8984/29/i=46/a=465901>
 - [76] Yamamoto T, Kanno R, Takeda Y, Yamamoto O, Kawamoto Y and Takano M 1994 *Journal of Solid State Chemistry* **109** 372–383
 - [77] Hamann D R 2013 *Phys. Rev. B* **88**(8) 085117 URL <https://link.aps.org/doi/10.1103/PhysRevB.88.085117>
 - [78] Perdew J P, Burke K and Ernzerhof M 1996 *Phys. Rev. Lett.* **77**(18) 3865–3868 URL <https://link.aps.org/doi/10.1103/PhysRevLett.77.3865>
 - [79] van Setten M, Giantomassi M, Bousquet E, Verstraete M, Hamann D, Gonze X and Rignanese G M 2018 *Computer Physics Communications* **226** 39 – 54 ISSN 0010-4655 URL <http://www.sciencedirect.com/science/article/pii/S0010465518300250>
 - [80] Capone M, de' Medici L and Georges A 2007 *Phys. Rev. B* **76**(24) 245116 URL <http://link.aps.org/doi/10.1103/PhysRevB.76.245116>
 - [81] Liebsch A and Ishida H 2012 *J. Phys.: Condens. Matter* **24** 053201 URL <http://stacks.iop.org/0953-8984/24/i=5/a=053201>
 - [82] Caffarel M and Krauth W 1994 *Phys. Rev. Lett.* **72**(10) 1545–1548 URL <http://link.aps.org/doi/10.1103/PhysRevLett.72.1545>